Research Square

Preprints are preliminary reports that have not undergone peer review.
They should not be considered conclusive, used to inform clinical practice,
or referenced by the media as validated information.

Characterization of mechanical properties and microstructure of non-equiatomic medium-entropy alloys Fe40Mn40Co10Cr10 and Fe50Mn30Co10Cr10 in different structural states over a large temperature range

Elena Tabachnikova

tabachnikova@scholar.org.ua

B.Verkin Institute for Low Temperature Physics and Engineering of the National Academy of Sciences of Ukraine

Sergii Shumilin
Igor Kolodiy
Tetiana Hryhorova
Yuri Semerenko
https://orcid.org/0000-0003-2268-0572
Serhii Smirnov
Ivan Kashuba
Yuriy Shapovalov
Tetiana Tykhonovska
Mykhailo Tikhonovsky
Yi Huang
Terence G. Langdon

Research Article

Keywords: medium-entropy alloy, mechanical properties, microstructure, TRIP, TWIP

Posted Date: February 24th, 2026

DOI: https://doi.org/10.21203/rs.3.rs-8936153/v1

License: This work is licensed under a Creative Commons Attribution 4.0 International License.
Read Full License

Additional Declarations: The authors declare no competing interests.

Characterization of mechanical properties and microstructure of non-equiatomic medium-entropy alloys $Fe_{40}Mn_{40}Co_{10}Cr_{10}$ and $Fe_{50}Mn_{30}Co_{10}Cr_{10}$ in different structural states over a large temperature range

E. Tabachnikova[1], S. Shumilin[1], I. Kolodiy[2], T. Hryhorova[1], Y. Semerenko[1], S. Smirnov[1], I. Kashuba[1], Y. Shapovalov[1], T. Tykhonovska[2], M. Tikhonovsky[2], Yi Huang[3], Terence G. Langdon[4]

[1]B.Verkin ILTPE of NASU, Kharkiv, Ukraine
[2]National Science Center "KIPT" of NASU, Kharkiv, Ukraine
[3]Department of Design and Engineering, Bournemouth University, Poole, UK
[4]Department of Aerospace & Mechanical Engineering, University of Southern California, USA

Keywords: medium-entropy alloy, mechanical properties, microstructure, TRIP, TWIP

Abstract. A comparative analysis was carried out to evaluate the low-temperature mechanical behavior and microstructural evolution of two non-equiatomic medium-entropy alloys: $Fe_{40}Mn_{40}Co_{10}Cr_{10}$ and $Fe_{50}Mn_{30}Co_{10}Cr_{10}$, examined in both coarse-grained (CG) and nanostructured states. The results demonstrate that, unlike the CG alloy, the NS counterparts undergo a complete phase transformation from the Face-Centered Cubic to the Hexagonal Close-Packed lattice. Notably, the fraction of the hcp phase in the nanostructured state shows only a weak dependence on temperature and on the number of rotations imposed during high-pressure torsion (HPT).
This finding highlights the fundamental role of severe plastic deformation in stabilizing the hcp phase, effectively overriding the temperature sensitivity observed in the coarse-grained alloys. The comparison underscores that nanostructuring not only alters the phase balance but also homogenizes the response of $Fe_{40}Mn_{40}Co_{10}Cr_{10}$ and $Fe_{50}Mn_{30}Co_{10}Cr_{10}$ alloys under cryogenic and ambient conditions, pointing to the dominant influence of grain refinement and defect density in driving phase stability.

Introduction

The enhancement of the physical and mechanical properties in a new class of materials - multicomponent high-entropy alloys (HEAs) [1-6] - was initially attributed [1, 2] to the increased configurational entropy of mixing compared with conventional multicomponent alloys. Early studies suggested that superior mechanical performance could be achieved only in equiatomic HEAs, for which the mixing entropy lies in the range of 13-19 J/(K·mol) and the number of constituent elements exceeds five.

Subsequent investigations [7-9], however, revealed that many non-equiatomic medium-entropy alloys (MEAs) containing fewer than five components also exhibit remarkable mechanical properties. This behavior is linked to the activation of additional deformation mechanisms, whose influence becomes particularly pronounced at reduced temperatures. Among these mechanisms are deformation twinning and strain-induced phase transformations, commonly referred to as TWIP and TRIP effects [7-9].

It has been demonstrated that in both coarse-grained [10, 11] and nanostructured [12] states, the $Fe_{40}Mn_{40}Co_{10}Cr_{10}$ MEA undergoes plastic deformation through the combined action of dislocation slip and twinning (TWIP), while the $Fe_{50}Mn_{30}Co_{10}Cr_{10}$ MEA exhibits transformation-induced plasticity (TRIP). As a result, these alloys display high strength and microhardness at low temperatures.

For the purpose of microstructural engineering, where achieving an optimal balance between strength and ductility is critical, it is therefore of considerable interest to compare the low-temperature mechanical properties and deformation mechanisms of TWIP and TRIP MEAs in different structural

states. This comparative analysis, which has not been available until now, forms the central aim of the present work.

Materials and methods of research

Coarse-grained (CG) non-equiatomic medium-entropy alloys $Fe_{40}Mn_{40}Co_{10}Cr_{10}$ (TWIP MEA) and $Fe_{50}Mn_{30}Co_{10}Cr_{10}$ (TRIP MEA) were synthesized by arc melting using alloying elements of purity exceeding 99.9 at.%. A detailed description of the alloy preparation procedure has been reported elsewhere [10].

To obtain the nanostructured state (NS), severe plastic deformation was applied by means of high-pressure torsion (HPT) at two temperatures, 300 K (RT-HPT) and 77 K (cryo-HPT). The shear strain values were calculated according to equation (1):

$$\gamma = 2\pi \frac{n \cdot r}{h}, \quad (1)$$

where r is the radial distance from the rotation axis, $h = 0.8$ mm is the sample thickness after HPT processing, ϕ is the angle of HPT and $n = \frac{\phi}{360^0}$ is the number of rotations on 360^0. The applied pressure was 2 GPa, and the number of rotations was set to 0.25 and 5. The methodology for producing nanostructured samples has been described in detail in earlier works [10, 12].

Mechanical testing in the initial coarse-grained state was performed on samples with dimensions of 16×3×0.4 mm, subjected to uniaxial tension at a constant strain rate of s over the temperature range 4.2-300 K. In the nanostructured state (after HPT at 300 K and 77 K), compression tests were conducted on samples cut from the edge regions of the disks, corresponding to the uniform deformation zone. These specimens, with dimensions of 0.6×0.6×1.2 mm, were deformed at 300 K and 77 K at the same relative loading rate of 10^{-4} s^{-1}.

Microhardness measurements in the nanostructured state were carried out using the Vickers indentation method. Two instruments were employed: the MHT-4 microscope (Anton Paar GmbH, Graz, Austria) with a load of 1.5 N, and the PMT-3 microhardness tester (Instrument-Making Plant, Moscow, USSR) with a load of 2 N, both at room temperature.

Microstructural characterization was performed by X-ray diffraction (XRD) using a Bruker D8 Discover diffractometer (Bruker AXS GmbH, Karlsruhe, Germany) with monochromatic Cu-Kα and Co-Kα radiation, as well as by scanning electron microscopy (SEM) with EBSD analysis using a Zeiss Supra 55 VP microscope.

The acoustic properties were examined using mechanical resonance spectroscopy, with the specimen electrostatically excited at a bending vibration frequency of approximately 400 Hz. Linear bending oscillations were studied under an amplitude-independent regime of acoustic strain, on the order of $\varepsilon_0 \sim 10^{-7}$. When subjected to a cyclic electric force, the thin plate underwent forced vibrations, with the excitation frequency f adjusted near the fundamental resonance f_r of its mechanical oscillations. As a result, the material experienced an alternating stress $\sigma = \sigma_0 \cdot \sin(\omega t)$ at the cyclic frequency $\omega = 2\pi f$, to which the specimen responded with a small cyclic deformation $\varepsilon_0 \cdot \sin(\omega t - \varphi)$. Due to the strain viscosity of the material, this deformation was phase-shifted relative to the applied stress by an angle φ. In this context, the dynamic elastic modulus is defined by the component of deformation that remains in phase with the applied stress. A detailed account of the experimental procedure is provided in references [13–16]. For a cantilevered specimen, the dynamic Young's modulus E is given by the following relation:

$$E = 38.3 \frac{\rho l^4}{s^2} \cdot f_r^2, \quad (2)$$

where s and l denote the specimen's thickness and length, respectively, and ρ its density. The numerical coefficient in equation (2) depends on both the specimen's geometry and the value of Poisson's ratio.

Mechanical testing was conducted using an MRK-3 deformation machine (ILTPE, Kharkiv, Ukraine).

Results and discussion

Structural characteristics of TWIP and TRIP MEAs in CG state

Fig. 1 and 2 show the X-Ray Diffraction (XRD) patterns of the structure of the CG TWIP and TRIP MEA**s** [10, 11].

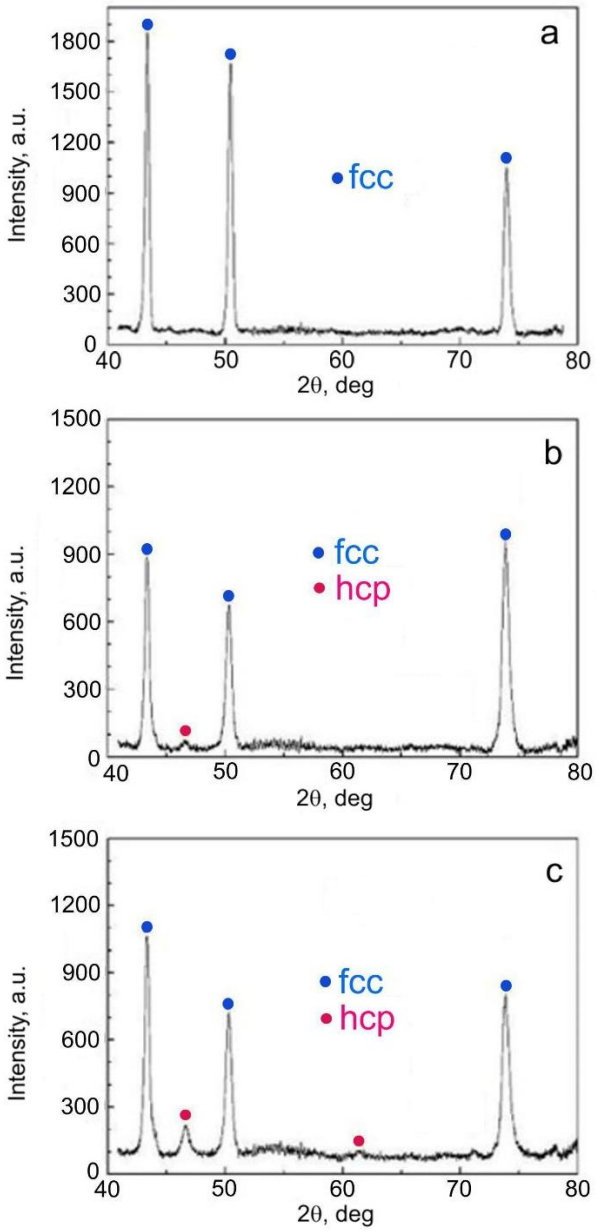


Fig. 1 XRD patterns of CG TWIP MEA in initial state and after deformation by tension to fracture at different temperatures: (a) - initial state, (b) - 295 K, (c) - 4.2 K.

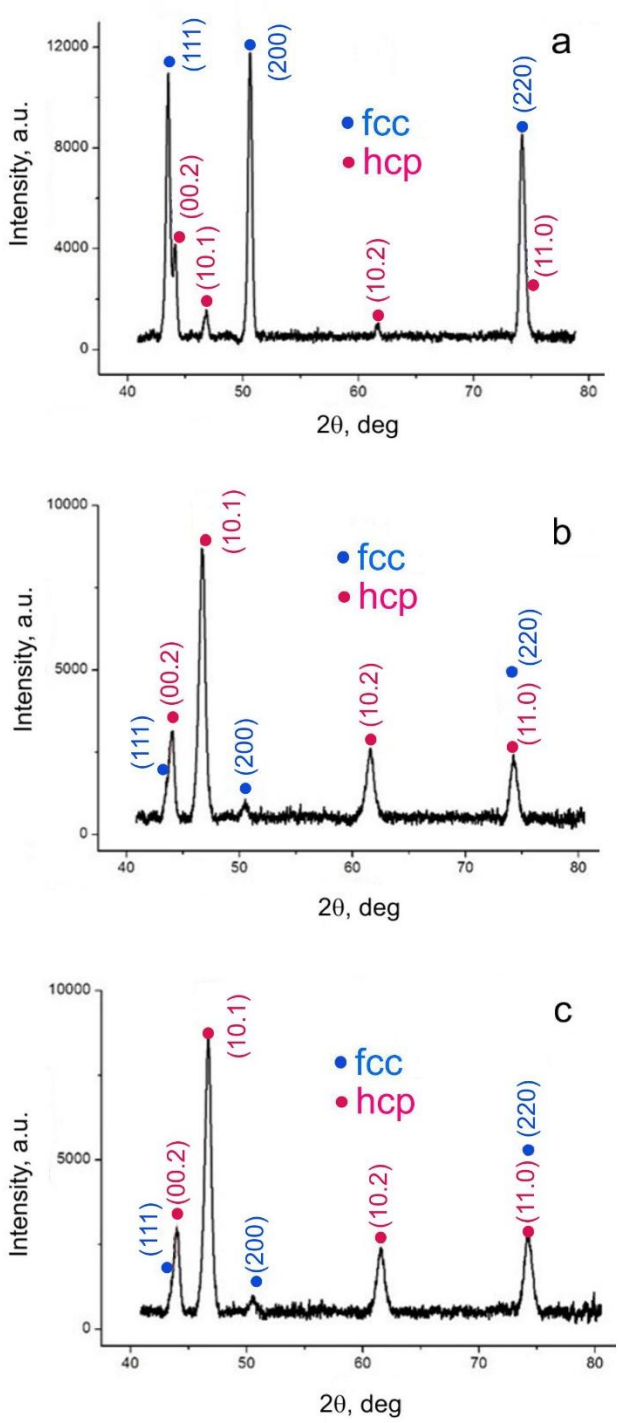


Fig 2 XRD patterns of CG TRIP MEA in initial state and after deformation by tension before failure at different temperatures: (a) – initial state, (b) - 295 K, (c) - 4.2 K.

As illustrated in Fig. 1a and Fig. 2a, the initial coarse-grained (CG) state of the TWIP-type medium-entropy alloy (MEA) is characterized by a single Face-Centered Cubic (fcc) phase. In contrast, the TRIP-type MEA exhibits a dual-phase structure consisting of both fcc and Hexagonal Close-Packed (hcp) phases. The relative intensity of the diffraction maxima reveals that the fcc lattice dominates in the TRIP alloy at this stage, with the ratio of peak heights $\frac{I_{fcc}}{I_{hcp}} \approx 6$.

Upon plastic deformation (Fig. 1), the initially single-phase fcc structure of the TWIP MEA transforms into a two-phase system. Moreover, when the temperature is reduced below 300 K, the

diffraction peaks associated with the hcp phase increase in intensity, indicating a growing fraction of this phase. These observations are consistent with earlier microscopic investigations of TWIP MEAs [11], which demonstrated that deformation leads to the formation of elongated grains whose size decreases from approximately 40 μm to 15-20 μm. In addition, those studies revealed that, alongside conventional dislocation slip, twinning dislocations emerge as a direct consequence of the TWIP mechanism.

Turning to Fig. 2, the TRIP MEA shows a different evolution. Its initial two-phase state undergoes significant redistribution during plastic deformation across all tested temperatures. The relative peak intensities shift to $\frac{I_{fcc}}{I_{hcp}} \approx 0.4$, signifying that the hcp phase becomes predominant in the alloy's microstructure. Comparable structural transformations have been reported previously for TRIP MEAs [17, 7], where progressive deformation was found to increase the hcp fraction dramatically. By the onset of necking in tensile specimens, the hcp phase content reached 75–90 wt%, underscoring the strong tendency of this alloy system to undergo strain-induced phase transformation.

Structural characteristics of TWIP and TRIP MEAs in NS state

The diffraction patterns of both alloys subjected to HTP at room and liquid nitrogen temperatures are shown in Fig. 3 and Fig. 4.

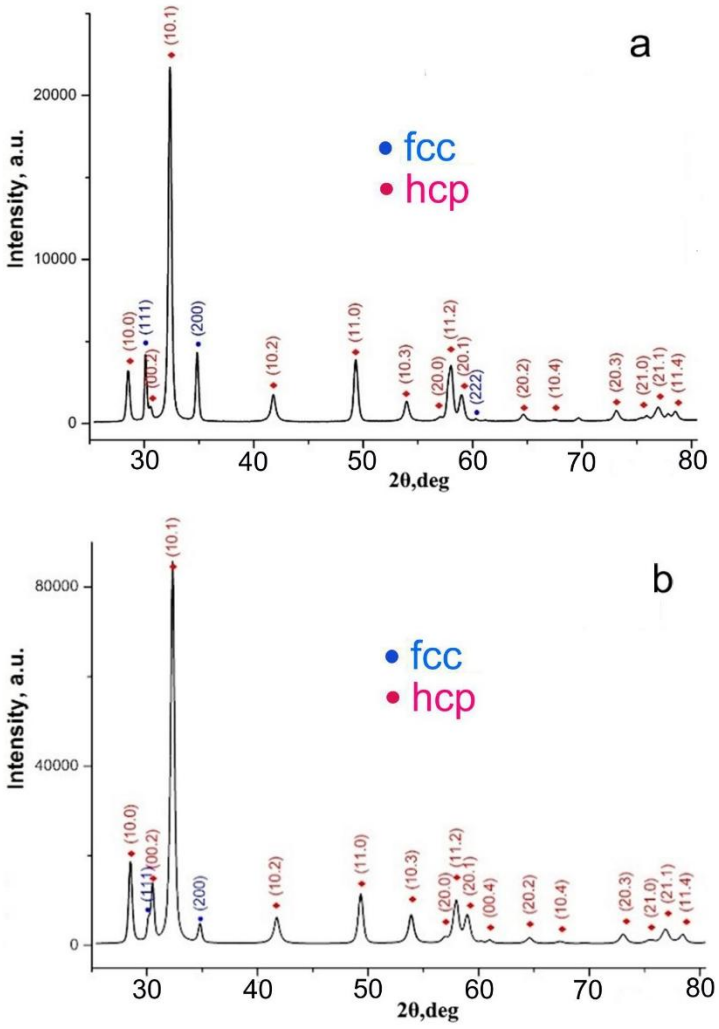


Fig. 3 XRD patterns of the TWIP MEA in the nanostructured state obtained by HPT (n = 5) at 300 K (RT-HPT) - (a) and 77 K (cryo-HPT) - (b).

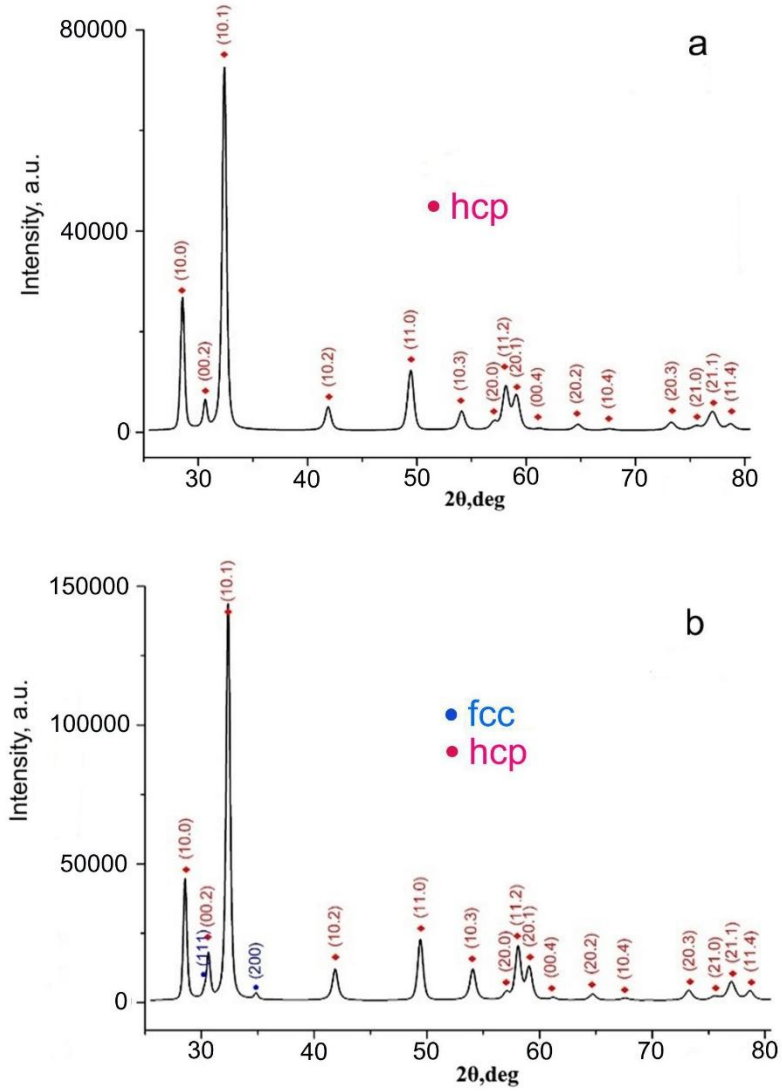


Fig. 4 XRD patterns of the TRIP MEA in the NS state obtained by HPT (n = 5) at 300 K (RT-HPT) - (a) and 77 K (cryo-HPT) - (b).

Figures 3 and 4 present the diffraction patterns of the alloys in their nanostructured states, obtained through high-pressure torsion (HPT) processing at 300 K and 77 K with five rotations (n = 5). As shown in Fig. 3, HPT deformation induces the coexistence of two phases fcc and hcp in both TWIP and TRIP MEAs. Remarkably, in one particular case, namely after room-temperature HPT at n = 5, the TRIP alloy exhibits a fully transformed structure consisting exclusively of the hcp phase (Fig. 4a).

It is noteworthy that in the nanostructured state, the relative intensities of the diffraction peaks corresponding to the hcp and fcc phases differ by nearly a factor of two. However, the processing temperature and the number of rotations during HPT exert only a minor influence on this ratio, suggesting that the phase balance is largely governed by the deformation mechanism itself rather than by external thermal conditions.

Figures 5 and 6 present EBSD orientation maps illustrating the evolution of the microstructure in coarse-grained TWIP and TRIP alloys under different structural states. The maps highlight the initial condition and the changes induced by deformation to fracture at various temperatures, with orientation shown in inverse pole figure (IPF) colors.

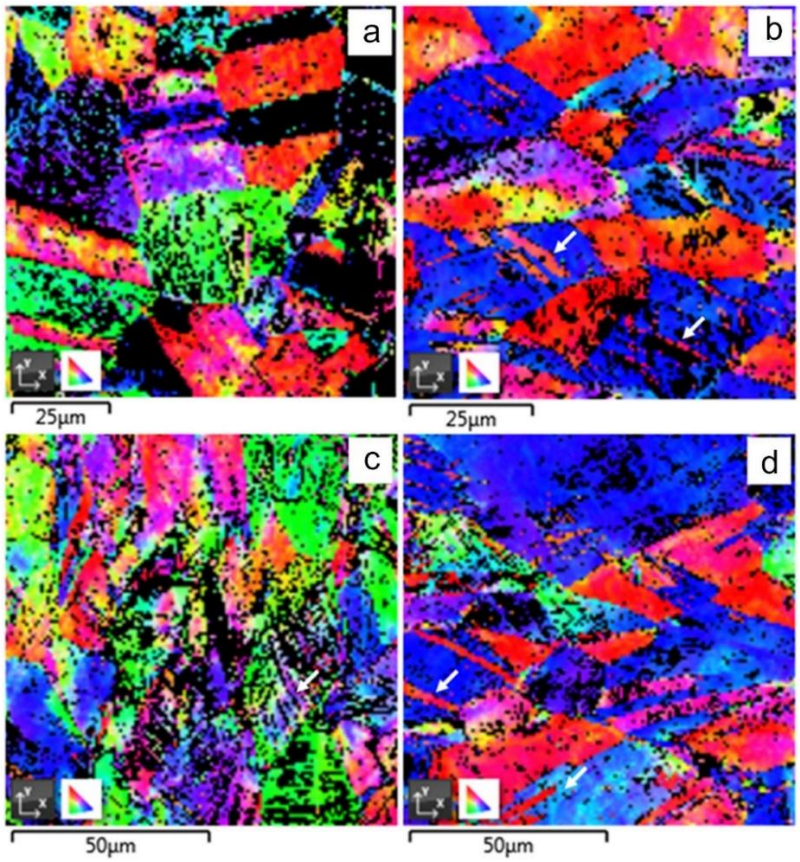


Fig. 5 Electron backscatter diffraction (EBSD) maps of the microstructure of the coarse-grained TWIP alloy in different structural states: (a) - initial condition; deformed to failure at various temperatures: (b) - 295 K, (c) - 77 K, (d) - 4.2 K. Orientation maps are shown in inverse pole figure (IPF) colors. Twins are marked with white arrows.

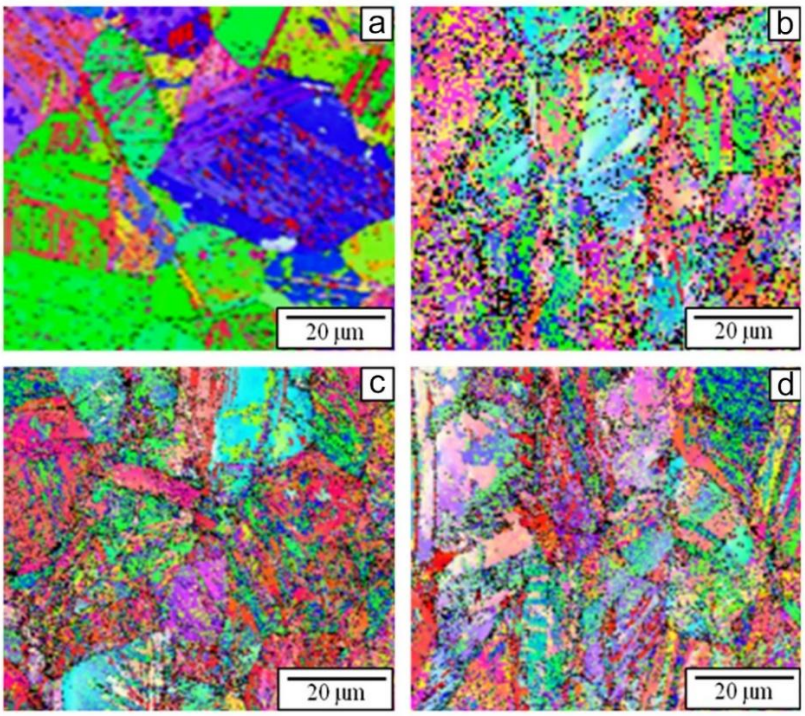


Fig. 6 EBSD maps of the coarse-grained TRIP alloy showing the evolution of the microstructure in different structural states: (a) before deformation; deformed to fracture at various temperatures: (b) 295 K, (c) 77 K, (d) 4.2 K. Orientation maps are presented in inverse pole figure (IPF) colors.

The detailed phase composition and structural parameters of the alloys, derived from quantitative analysis of the diffraction curves, are summarized in Table 1. These results highlight the pronounced stability of the hcp phase in TRIP alloy under severe plastic deformation, as well as the tendency of TWIP alloy to retain a mixed-phase structure even in the nanostructured regime.

Table 1

Phase composition and structural characteristics (microhardness H_v, crystallite size D, microstrain <ε>, twin faults probability β) of the studied TRIP and TWIP alloys after RT-HPT and cryo-HPT for the number of rotations $n = 0.25$ ($\gamma = 8.84$) and $n = 5$ ($\gamma = 177$). The H_v and γ values given for a distance at $r = 4.5$ mm from the center of the samples. Dashes correspond to the cases when the structural characteristics could not be determined. The microstructural characteristics for the TWIP and TRIP alloys in the initial state are taken from [10, 11].

Sample				H_v, GPa	Phase fraction, vol%		Lattice parameters, Å	Structural characteristics		
								D, nm	10^3<ε>	10^3β
CG	TWIP			1.3	hcp	0	-	-	-	-
					fcc	100	3.624			
	TRIP			2.5	hcp	41	a = 2.542 c = 4.104	-	-	-
					fcc	59	3.604	215	<0.50	
NS	TWIP	$n = 0.25$ $(\phi = 90^0)$	RT-HPT	4.2	hcp	84	a = 2.546 c = 4.114	49	2.24	4.1
					fcc	16	3.608	87	1.95	-
			cryo-HPT	4.3	hcp	96	a = 2.546 c = 4.113	42	3.40	6.9
					fcc	4	3.611	-	-	-
		$n = 5$ $(\phi = 1800^0)$	RT-HPT	4.8	hcp	82	a = 2.546 c = 4.113	54	2.24	4.3
					fcc	18	3.609	75	1.66	-
			cryo-HPT	5.4	hcp	94	a = 2.547 c = 4.122	42	2.96	6.8
					fcc	6	3.613	34	1.64	-
	TRIP	$n = 0.25$ $(\phi = 90^0)$	RT-HPT	4.4	hcp	90	a = 2.544 c = 4.103	54	2.99	5.2
					fcc	10	3.601	43	1.78	-
			cryo-HPT	4.9	hcp	97	a = 2.543 c = 4.099	44	3.64	6.4
					fcc	3	3.598	-	-	-
		$n = 5$ $(\phi = 1800^0)$	RT-HPT	5.2	hcp	100	a = 2.543 c = 4.106	43	4.03	4.1
					fcc	0	-			
			cryo-HPT	5.6	hcp	98	a = 2.543 c = 4.106	60	3.45	5.4
					fcc	2	3.605	-	-	-

From the data Table 1 summarized in Fig. 7, it becomes clear that high-pressure torsion (HPT) processing of both TWIP and TRIP medium-entropy alloys (MEAs) results in an almost complete phase transformation from the fcc lattice to the hcp lattice. Importantly, the fraction of the hcp phase shows only a weak dependence on either the HPT temperature or the number of rotations *n* applied during deformation.

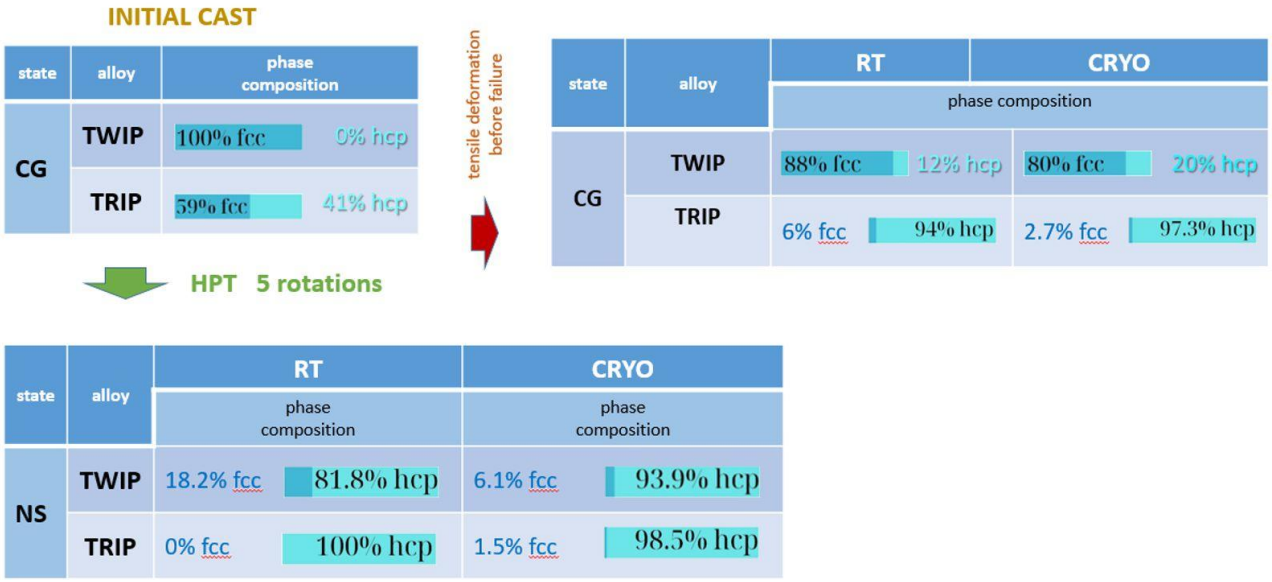


Fig. 7 Phase composition evolution during structural state changes in TWIP and TRIP MEAs.

A consistent trend is observed across all experimental conditions: lowering the temperature and increasing the number of rotations during HPT lead to a rise in the Vickers hardness H_v values. Furthermore, after HPT deformation, the differences in phase composition between TWIP and TRIP alloys diminish compared to their coarse-grained counterparts. This convergence is particularly pronounced in the TWIP alloy, where the reduction in phase disparity is more significant than in the TRIP alloy.

Overall, the presented results demonstrate that HPT deformation induces complex structural modifications in both alloy systems, with the extent of transformation governed jointly by temperature and strain level. The findings also confirm that, regardless of the deformation mode - whether HPT or tensile loading over a broad temperature range - the alloys undergo a phase transition from fcc to hcp. This transformation is closely linked to the stacking fault energy (SFE) [7, 9, 18], which dictates the stability of the fcc lattice. For TRIP MEA ($Fe_{50}Mn_{30}Co_{10}Cr_{10}$), the SFE at room temperature is approximately 18 mJ/m, and the Gibbs free energy change associated with the fcc → hcp transformation is negative, favoring the hcp phase.

It is also well established that grain boundaries act as nucleation sites for hcp phase formation, and their volume fraction increases substantially during severe plastic deformation. Moreover, both TWIP and TRIP mechanisms become more active at lower temperatures, as the energy barrier for transformation from the metastable fcc phase to the energetically more stable hcp phase decreases. This explains the enhanced phase transition observed under cryogenic conditions.

Acoustic properties of TWIP and TRIP MEAs in the CG state

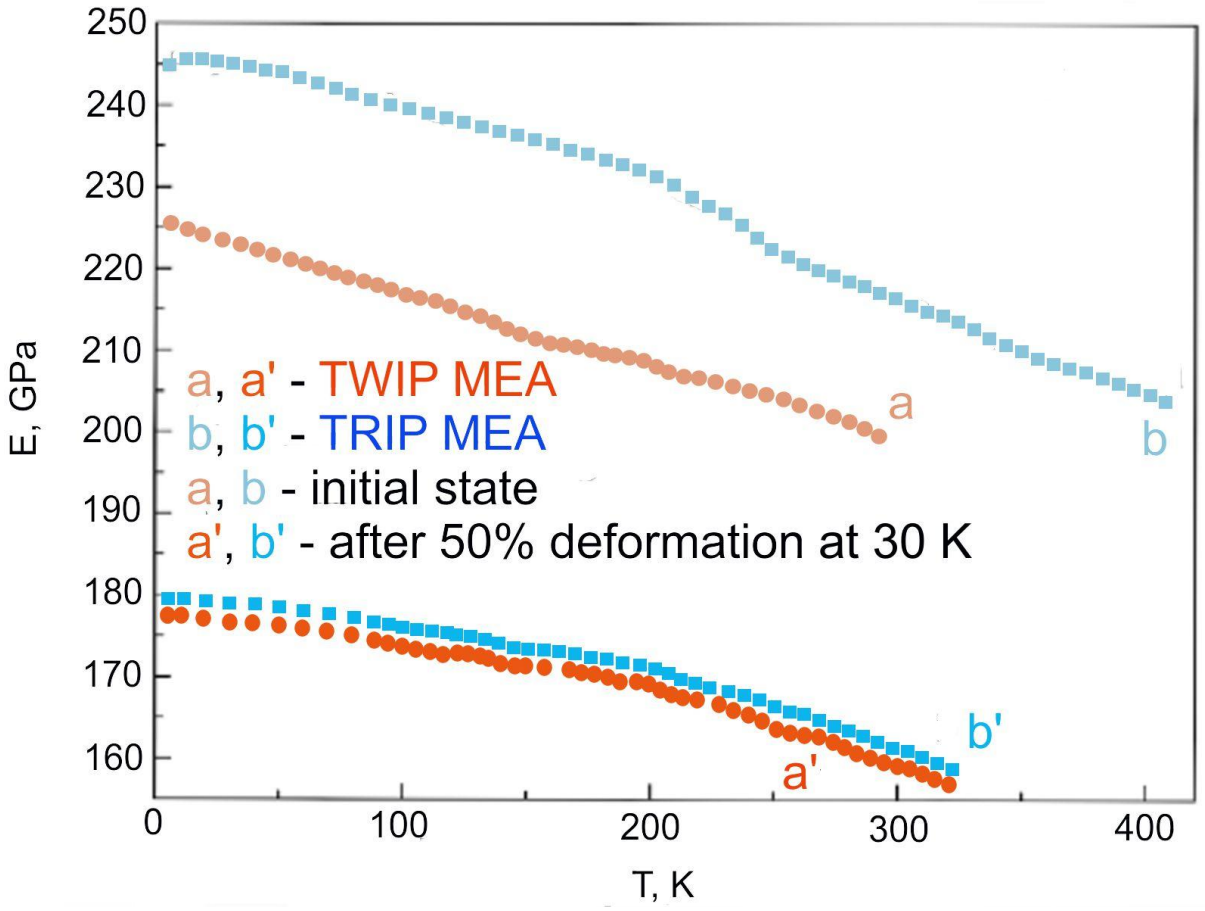


Fig. 8 Temperature dependences of the dynamic Young's modulus both in the initial (a – TRIP MEA; a' – TWIP MEA) and in the deformed CG state (b – TRIP MEA; b' – TWIP MEA).

As shown in Fig. 8, the temperature dependence of the dynamic Young's modulus E(T) was measured for both TRIP and TWIP MEAs in their initial states (a, b) and after tensile deformation up to 50% at 30 K (a′, b′), covering a broad temperature range. The results reveal that, in both the undeformed and deformed conditions, the modulus decreases monotonically with increasing temperature, dropping by approximately 10% between 4.2 K and 300 K.

A striking observation is that tensile deformation of 50% at 30 K leads to a substantial reduction in the absolute values of the modulus across the entire temperature interval studied. This pronounced decrease can be attributed to microstructural changes induced by deformation, particularly the growth of the hcp phase at the expense of the fcc phase. Such phase evolution directly influences the elastic response of the alloys.

It is also noteworthy that, in the deformed state (Fig. 8 a′ and b′), the temperature dependence of the elastic modulus for TRIP and TWIP MEAs nearly coincides. This convergence suggests that once deformation has driven significant phase transformation, the mechanical response of the two alloy systems becomes essentially similar, despite their different initial phase compositions.

Mechanical characteristics of TWIP and TRIP MEAs in CG and NS states under active loading

The coarse-grained state

Table 2 show the parameters of the deformation curves, obtained during uniaxial tension of MEA CG TWIP and TRIP alloys. From the data presented in Table 2, it is evident that in both alloys, when

the temperature decreases from 300 K to 4.2 K, a significant increase in both the yield strength and the ultimate strength is observed, which is characteristic of thermally activated plastic deformation [19, 20]. It should also be noted that from the data presented it follows that in the temperature range from room temperature to helium temperature the CG TRIP MEA demonstrates higher ultimate strength compared to the CG TWIP MEA, while maintaining sufficiently high plasticity in both alloys.

Table 2

Cryogenic plasticity characteristics of the CG TWIP and TRIP MEAs

		T, K					
		0.5	4.2	30	77	150	295
Yield strength $\sigma_{0.2}$, MPa	CG TWIP MEA	543	579	550	414	324	191
	CG TRIP MEA	536	606	586	450	-	230
Ultimate strength σ_u, MPa	CG TWIP MEA	1690	1805	-	1710	1452	746
	CG TRIP MEA	1274	1513	1452	1384	-	758
Uniform elongation ε, %	CG TWIP MEA	43	45.6	-	46	50	46
	CG TRIP MEA	54	47	47	48	-	50

This table presents the key parameters describing the plastic response of the alloys under cryogenic conditions. The comparison highlights the distinct deformation mechanisms active in each system: twinning-induced plasticity (TWIP) in $Fe_{40}Mn_{40}Co_{10}Cr_{10}$, and transformation-induced plasticity (TRIP) in $Fe_{50}Mn_{30}Co_{10}Cr_{10}$. The data emphasize how cryogenic temperatures influence ductility, strength, and phase stability, providing insight into the fundamental differences between the two alloys. By quantifying cryogenic plasticity characteristics, Table 2 underscores the role of low-temperature deformation in promoting either twinning or phase transformation, thereby shaping the mechanical behavior of CG TWIP and TRIP alloys. These results form the basis for understanding how structural state and deformation mechanisms interact to determine alloy performance under extreme conditions.

The nanostructured (NS) state

The mechanical properties of the TWIP alloy in the nanostructured state were investigated under uniaxial compression at a constant strain rate of 10^{-4} s^{-1}, for deformation temperatures of 300 K and 77 K. The nanostructured state was obtained by high-pressure torsion (HPT) performed at two processing temperatures: 300 K (RT-HPT) and 77 K (cryo-HPT).

Table 3 presents the parameters of the deformation curves - yield strength $\sigma_{0.2}$, uniform elongation ε, ultimate strength σ_u - measured during compression of the medium-entropy nanostructured TWIP alloy. For comparison, the table also includes the corresponding values for samples in the coarse-grained state [11].

The results clearly demonstrate that the transition from the coarse-grained to the nanostructured state leads to a substantial increase in both yield strength and ultimate strength, accompanied by a reduction in plasticity. In contrast, the nanostructured TRIP MEA exhibits a complete loss of plasticity under uniaxial compression at 300 K, with samples failing already in the elastic region.

Fractographic observations reveal the formation of major cracks aligned with the loading axis, accompanied by numerous smaller lateral cracks.

This pronounced brittleness in the nanostructured TRIP alloy is evidently linked to the increased fraction of grain boundaries in the NS state, which prevents the effective transfer of plastic deformation from grain to grain. By comparison, the TWIP alloy retains a measurable plasticity resource even after nanostructuring, underscoring the fundamental difference in deformation mechanisms between TWIP and TRIP systems.

Table 3

Mechanical properties of the TWIP alloy in the nanostructured state, tested under uniaxial compression at a constant strain rate of 10^{-4} s^{-1}, for deformation temperatures of 300 K and 77 K. The nanostructured state was obtained by high-pressure torsion (HPT) carried out at two different processing temperatures: 300 K (RT-HPT) and 77 K (cryo-HPT)

	Structure state					
	Initial		RT-HPT		cryo-HPT	
	deformation temperature, K		deformation temperature, K		deformation temperature, K	
	77	300	77	300	77	300
Yield strength $\sigma_{0.2}$, MPa	0.41	0.19	1.97	1.49	2.17	1.62
Ultimate strength σ_u, MPa	1.71	0.75	2.32	1.82	2.38	1.84
Deformation to failure ε, %	46	46	5.15	5.38	3.5	6.62

This table summarizes the influence of both deformation temperature and HPT processing conditions on the mechanical response of the TWIP alloy. The comparison between RT-HPT and cryo-HPT samples highlights the role of cryogenic processing in enhancing strength and hardness, while maintaining the alloy's ductility under compression. The data provide a quantitative basis for understanding how severe plastic deformation at different temperatures modifies the mechanical behavior of TWIP alloys in the nanostructured regime.

Conclusions

The comprehensive investigation of the mechanical and acoustic properties of TWIP and TRIP alloys in both coarse-grained (CG) and nanostructured (NS) states allows us to draw several important conclusions:

1. Thermally activated plasticity. Both TWIP and TRIP alloys exhibit a thermally activated character of plastic deformation, regardless of whether they are in the CG or NS state.
2. Phase evolution under compression. In the undeformed TWIP alloy, the initially single-phase fcc structure transforms into a mixed fcc-hcp state during compression to failure, driven by the activation of twinning processes. This transformation is strongly enhanced as the deformation temperature decreases from 300 K to 4.2 K. In contrast, the undeformed TRIP alloy, which initially contains 59% fcc and 41% hcp phases, undergoes an almost complete transformation into a single-phase hcp structure (≈97% hcp) during compression, largely independent of temperature in the range 4.2-300 K.
3. Nanostructured alloys. In NS TWIP and NS TRIP alloys, unlike their CG counterparts, a complete phase transition from fcc to hcp is observed. The fraction of the hcp phase shows little sensitivity to either the HPT temperature or the number of rotations applied.

4. Microhardness increase. HPT deformation significantly raises the microhardness (H_v) of both alloys, with the effect being more pronounced in TWIP than in TRIP alloys. Lowering the HPT temperature from 300 K to 77 K further increases H_v in both systems.
5. Ductility differences. The NS TWIP MEA retains ductility under active compression at both 300 K and 77 K, whereas the NS TRIP alloy shows no macroscopic plasticity under similar conditions, highlighting a fundamental difference in mechanical response.
6. Elastic modulus reduction. Tensile deformation of 50% at 30 K in both CG TRIP and CG TWIP alloys leads to a marked reduction in the absolute values of the dynamic Young's modulus across the entire temperature range studied. This decrease is attributed to microstructural changes, particularly the growth of the hcp phase induced by deformation.

Acknowledgments

This work was partly supported by the Projects No.0124U000272 of the National Academy of Sciences of Ukraine.

Reference

[1] J.W. Yeh, S.K. Chen, S.J. Lin, J.Y. Gan, T.S. Chin, T.T. Shun, C.H. Tsau, S.Y. Chang, Nanostructured high-entropy alloys with multiple principal elements: Novel alloy design concepts and outcomes, Adv. Eng. Mater. 6 (2004) 299–303. DOI: 10.1002/adem.200300567
[2] B. Cantor, I.T.H. Chang, P. Knight, A.J.B. Vincent, Microstructural development in equiatomic multicomponent alloys, Mater. Sci. Eng. A375–377 (2004) 213–218. DOI: 10.1016/j.msea.2003.10.257
[3] E.P. George, D. Raabe, R.O. Ritchie, High-entropy alloys, Nat. Rev. Mater. 4(8) (2019) 515–534. DOI: 10.1038/s41578-019-0121-4
[4] N.T.C. Nguyen, P. Asghari-Rad, P. Sathiyamoorthi, A. Zargaran, C.S. Lee, H.S. Kim, Ultrahigh high-strain-rate superplasticity in a nanostructured high-entropy alloy, Nat. Commun. 11 (2020) 2736. DOI: 10.1038/s41467-020-16601-1
[5] W. Li, D. Xie, D. Li, Y. Zhang, Y. Gao, P.K. Liaw, Mechanical behavior of high-entropy alloys, Prog. Mater. Sci. 118 (2021) 100777. DOI: 10.1016/j.pmatsci.2021.100777
[6] H. Shahmir, M.S. Mehranpour, S.A.A. Shams, T.G. Langdon, Twenty years of the CoCrFeNiMn high-entropy alloy: Achieving exceptional mechanical properties through microstructure engineering, J. Mater. Res. Technol. 23 (2023) 3362–3423. DOI: 10.1016/j.jmrt.2023.01.181
[7] Z. Li, K.G. Pradeep, Y. Deng, D. Raabe, C.C. Tasan, Metastable high-entropy dual-phase alloys overcome the strength–ductility trade-off, Nature 534(7606) (2016) 227–230. DOI: 10.1038/nature17981
[8] Z. Wang, W. Lu, D. Raabe, Z. Li, On the mechanism of extraordinary strain hardening in an interstitial high-entropy alloy under cryogenic conditions, J. Alloys Compd. 781 (2019) 734–743. DOI: 10.1016/j.jallcom.2018.12.061
[9] S. Yang, Y. Yang, H. Wang, The characteristic and thermodynamics/kinetics of martensitic transformation in $Fe_{50}Mn_{30}Co_{10}Cr_{10}$ high-entropy alloy during deformation/heat treatment, Adv. Eng. Mater. 22(3) (2020) 1900868. DOI: 10.1002/adem.201900868
[10] T.V. Hryhorova, S.E. Shumilin, Y.O. Shapovalov, Y.O. Semerenko, O.D. Tabachnikova, M.A. Tikhonovsky, A.S. Tortika, M.J. Zehetbauer, E. Schafler, Structure and properties of high-entropy alloys, V.N. Karazin Natl. Univ. Ser. Phys. 32 (2020) 41. DOI: 10.26565/2222-5617-2020-32-05
[11] E.D. Tabachnikova, T.V. Hryhorova, S.E. Shumilin, I.V. Kolodiy, Y.O. Shapovalov, Y.O. Semerenko, S.N. Smirnov, I.V. Kashuba, M.A. Tikhonovsky, M.I. Zehetbauer,

E. Schafler, Low-temperature deformation behavior of high-entropy alloys, Low Temp. Phys. 48 (2022) 845. DOI: 10.1063/10.0014029
[12] E.D. Tabachnikova, T.V. Hryhorova, S.N. Smirnov, I.V. Kolodiy, Y.O. Shapovalov, A.V. Levenets, S.E. Shumilin, I.V. Kashuba, M.A. Tikhonovsky, F. Spieckermann, M.J. Zehetbauer, E. Schafler, Y. Huang, T.G. Langdon, Structure and cryogenic mechanical properties of severely deformed nonequiatomic alloys of Fe-Mn-Co-Cr system, Low Temp. Phys. 49(11) (2023) 1294-1305. DOI: 10.1063/10.0021377
[13] Y.A. Semerenko, Interfacing the instrumental GPIB with a personal computer through the LPT port, Instrum. Exp. Tech. 48 (2005) 608–610. DOI: 10.1007/s10786-005-0107-x
[14] V.D. Natsik, Y.A. Semerenko, Dislocation mechanisms of low-temperature acoustic relaxation in iron, Low Temp. Phys. 45(5) (2019) 551–567. DOI: 10.1063/1.5097366
[15] Y.A. Semerenko, V.D. Natsik, Low temperature peak of internal friction in high-entropy $Al_{0.5}$CoCrCuFeNi alloy, Low Temp. Phys. 46(1) (2020) 78–86. DOI: 10.1063/10.0000367
[16] V.D. Natsik, Yu.A. Semerenko, Analysis of low-temperature relaxation resonances in materials containing defects. Functional Materials 11(2) (2004) 327–333.
[17] D. Li, Z. Li, L. Xie, Y. Zhang, W. Wang, Cryogenic mechanical behavior of a TRIP-assisted dual-phase high-entropy alloy, Nano Res. (2022) 1–8. DOI: 10.1007/s12274-021-3719-y
[18] Z. Li, C.C. Tasan, K.G. Pradeep, D. Raabe, A TRIP-assisted dual-phase high-entropy alloy: Grain size and phase fraction effects on deformation behavior, Acta Mater. 131 (2017) 323–335. DOI: 10.1016/j.actamat.2017.03.069
[18] V.D. Natsik, On strain delay time at the superconducting transition, Phys. Status Solidi A14 (1972) 271–275. DOI: 10.1002/pssa.2210140133
[20] V.L. Indenbom, Yu.Z. Estrin, Breakaway of dislocation from point defect treated as a stochastic problem, Phys. Status Solidi A 4 (1971) K37–K39. DOI: 10.1002/pssa.2210040139

Supplementary Files

This is a list of supplementary files associated with this preprint. Click to download.

- Abstract.jpg